

This manuscript has been authored by UT-Battelle, LLC under Contract No. DE-AC05-00OR22725 with the U.S. Department of Energy. The United States Government retains and the publisher, by accepting the article for publication, acknowledges that the United States Government retains a non-exclusive, paid-up, irrevocable, world-wide license to publish or reproduce the published form of this manuscript, or allow others to do so, for United States Government purposes. The Department of Energy will provide public access to these results of federally sponsored research in accordance with the DOE Public Access Plan (<http://energy.gov/downloads/doe-public-access-plan>).

Magnetic Excitations of the Hybrid Multiferroic $(\text{ND}_4)_2\text{FeCl}_5\cdot\text{D}_2\text{O}$

Xiaojuan Bai,^{1,*} Randy S. Fishman,² Gabriele Sala,¹ Daniel M. Pajerowski,¹ V. Ovidiu Garlea,¹ Tao Hong,¹ Minseong Lee,³ Jaime A. Fernandez-Baca,¹ Huibo Cao,¹ and Wei Tian^{1,†}

¹*Neutron Scattering Division, Oak Ridge National Laboratory, Oak Ridge, Tennessee 37831, USA*

²*Materials Science and Technology Division, Oak Ridge National Laboratory, Oak Ridge, Tennessee 37831, USA*

³*National High Magnetic Field Laboratory, Los Alamos National Laboratory, Los Alamos, New Mexico 87545, US*

(Dated: February 8, 2022)

We report a comprehensive inelastic neutron scattering study of the hybrid molecule-based multiferroic compound $(\text{ND}_4)_2\text{FeCl}_5\cdot\text{D}_2\text{O}$ in the zero-field incommensurate cycloidal phase and the high-field quasi-collinear phase. The spontaneous electric polarization changes direction concurrently with the field-induced magnetic transition, from mostly aligned with the crystallographic a -axis to the c -axis. To account for such change of polarization direction, the underlying multiferroic mechanism is believed to switch from the inverse Dzyaloshinskii–Moriya model to the p - d hybridization model. We perform a detailed analysis of the inelastic neutron data of $(\text{ND}_4)_2\text{FeCl}_5\cdot\text{D}_2\text{O}$ using linear spin-wave theory to investigate possible impact of different multiferroic mechanisms on the microscopic magnetic interactions. Our result reveals that the spin dynamics of both multiferroic phases can be well-described by a Heisenberg Hamiltonian with an easy-plane anisotropy. We find notable differences between the optimal model parameters of the two phases. In particular, the value of single-ion anisotropy shows a $\sim 50\%$ increase in the high-field phase. Nevertheless, the hierarchy of exchange strength and the balance among frustrated interactions do not change qualitatively between two phases, suggesting that magnetic interactions in $(\text{ND}_4)_2\text{FeCl}_5\cdot\text{D}_2\text{O}$ are much more robust than the electric polarization in response to delicate reorganizations of the electronic degrees of freedom in an applied magnetic field.

Crystalline condensed matter systems are assemblies of lattice, charge and spin degrees of freedoms with a hierarchy of complex interactions. In thermal equilibrium, materials may display various linear responses to small external stimuli, such as strain to stress, polarization to electric fields and magnetization to magnetic fields. A cross coupling of polarization (magnetization) with a magnetic (electric) field is generally referred as the magnetoelectric effect [1]. Single-phase magnetoelectric materials that host both ferroelectric order and (anti)ferromagnetic order are called multiferroics [2]. Understanding microscopic instabilities that give rise to these coupled phenomena is of fundamental interest.

Ferroelectric order requires breaking the spatial inversion symmetry. This can be achieved by a polar distortion driven by a structural instability, such as in BiFeO_3 where the major source of polarization is produced by Bi^{3+} displacements [3]. The long-range magnetic ordering in this material occurs on a different site [4], Fe^{3+} , and at a temperature ~ 460 K lower than the ferroelectric ordering $T_{\text{FE}} \approx 1103$ K. Although two types of order coexist in BiFeO_3 , they are of completely different origins and separated in energy scales. As a result, the coupling between them is quite weak. This is the typical case for so-called type-I (or proper) multiferroics. In comparison, type-II (or improper) multiferroics [5, 6], such as TbMnO_3 , are known for their strong magnetoelectric coupling effect which is driven by correlated electronic degrees of freedom. The spatial inversion symmetry in TbMnO_3 is broken by the formation of a cycloidal spin structure and the electric polarization is created by the lattice response to magnetic frustration through the

inverse Dzyaloshinskii–Moriya (DM) mechanism [7, 8]. Naturally, in this case, ferroelectric ordering is strongly coupled with magnetic ordering. The direction of the electric polarization is completely switchable by rotating the spiral plane in an applied magnetic field [9]. Meanwhile, chiral magnetic domains can also be selected by poling electric fields [10]. However, the absolute magnitude of the polarization in TbMnO_3 is rather small [9], only $\sim 0.1\%$ of BiFeO_3 , and the transition takes place at a much lower temperature, $T_{\text{FE}} \approx 28$ K.

The intimate coupling between ferroelectricity and magnetism in multiferroics provides a new knob to tune materials across quantum phase transition [11], realizing novel emergent phases. The progress of multiferroic research is heavily driven by discoveries of new materials. Most known multiferroic compounds are transition metal oxides, such as TbMnO_3 [8–10, 12–16], MnWO_4 [17], $\text{Ni}_3\text{V}_2\text{O}_8$ [18], CuO [19] and LiCuVO_4 [20], to name some that have spiral spin order [21]. The discovery of multiferroic behavior in crystalline molecule-based magnets and metal-organic framework materials (MOFs) has significantly expanded our horizon [22–25]. Structurally, such hybrid magnets consist of “hard” polyhedron building blocks bridged by “soft” organic linkers. This unique combination makes their magnetic properties highly tailorable. One can manipulate interaction pathways, spin anisotropy and effective dimensionality via ligand engineering. Interesting new phases can be readily stabilized with modest fields and pressures. Therefore, hybrid molecule-based multiferroics are an excellent platform to explore new physics, as well as to develop next-generation multi-functional devices.

The linear magnetoelectric response was recently discovered in the molecule-based compounds $A_2[\text{FeCl}_5 \cdot \text{H}_2\text{O}]$, $A = \text{K}, \text{Rb}$ or Cs [26]. The crystal structure of this family of compounds consists of distorted $[\text{FeCl}_5 \cdot \text{H}_2\text{O}]^{2-}$ octahedra linked by a network of hydrogen bonds [27]. A single magnetic ordering transition was observed in all three compounds at temperatures ranging from 14 to 4.5 K. Electric polarization can be induced in the ordered phases by applying an external magnetic field [26]. Interestingly, these materials transform into a multiferroic when the alkali metals are replaced by ammonium cations $[\text{NH}_4]^+$ [28]. In this case, electric polarization emerges *spontaneously* in zero field at the onset of the low-temperature cycloidal magnetic ordering – a key difference with linear magnetoelectric materials. Comprehensive thermodynamic measurements reveal rich multiferroic phase diagrams in an applied magnetic field along the crystallographic a - and c -axis, while the b -axis is the magnetic hard axis [28, 29]. The magnetic structures in different phases were solved from single crystal neutron diffraction using deuterated samples [30–33].

$(\text{NH}_4)_2\text{FeCl}_5 \cdot \text{H}_2\text{O}$ undergoes three transitions *en route* to multiferroicity in zero field. First, a structural transition occurs at $T_S \approx 79$ K. The crystal symmetry is lowered from orthorhombic $Pnma$ to monoclinic $P112_1/a$ with detectable $\sim 0.1^\circ$ change in one of the cell angles. This change is associated with an orientational ordering of $[\text{ND}_4]^+$ groups [33], Fig. 1(a). Next, a long-range magnetic ordering takes place at $T_N \approx 7.3$ K, stabilizing a collinear sinusoidal structure with magnetic moments along the a -axis [34]. At $T_{FE} \sim 6.8$ K, the magnetic structure changes to an incommensurate cycloid in the ac -plane with propagation vector $\mathbf{k} = (0, 0, 0.23)$, Fig. 1(b). At the same time, a spontaneous electric polarization emerges along \mathbf{a} . The magnitude of this polarization is quite small at $T = 3$ K, only $\sim 1\%$ of the polarization in TbMnO_3 . The direction of the polarization is consistent with the prediction of the inverse DM mechanism, $\mathbf{P} \sim \mathbf{r}_{ij} \times (\mathbf{S}_i \times \mathbf{S}_j)$, where $\mathbf{S}_i \times \mathbf{S}_j // \mathbf{b}$ and $\mathbf{r}_{ij} // \mathbf{c}$, therefore $\mathbf{P} // \mathbf{a}$.

A spin-flop transition occurs in the multiferroic phase of $(\text{NH}_4)_2\text{FeCl}_5 \cdot \text{H}_2\text{O}$ at $B \approx 5$ T when the field is along the a -axis, resulting in a $\mathbf{k} = \mathbf{0}$ quasi-collinear magnetic structure, Fig. 1(b). Similar transition happens at a lower field of $B \approx 3.5$ T when field is applied along the c -axis [28, 29]. In both cases, the electric polarization rotates to the c -axis and increases linearly up to the highest field of $B = 14$ T in the measurement. The spin-current inverse DM model can no longer explain the observed electric polarization in these spin-flop phases. Surprisingly, a spin-dependent p - d hybridization model can produce a non-vanishing polarization along the c -axis in both cases, based on the local environment of Fe^{3+} and the canted spin structure [31].

It is rather unusual to have two unrelated mechanisms

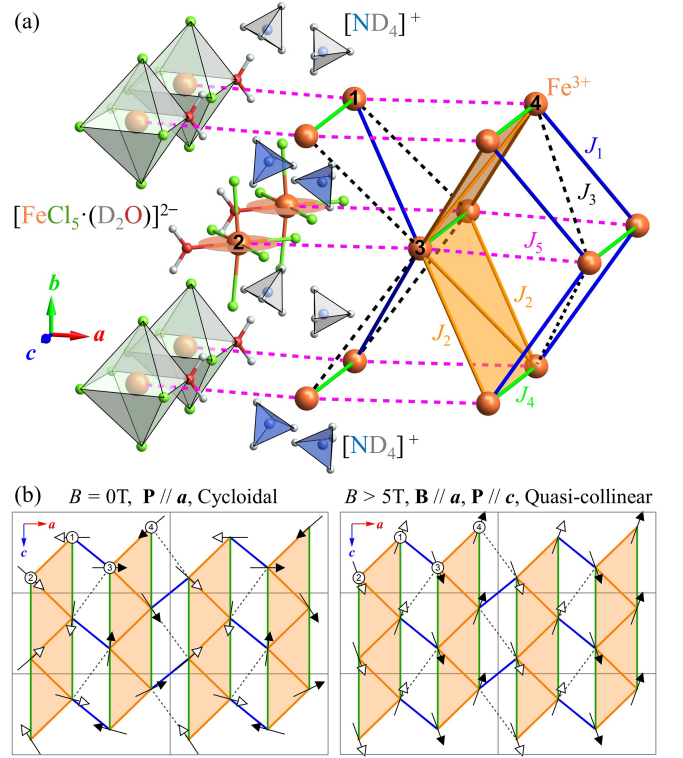


FIG. 1. Low-temperature crystal and magnetic structures determined by neutron diffraction study using deuterated $(\text{ND}_4)_2\text{FeCl}_5 \cdot \text{D}_2\text{O}$. (a) Partial crystal structure and magnetic exchange pathways of $(\text{ND}_4)_2\text{FeCl}_5 \cdot \text{D}_2\text{O}$ below the structural transition at $T_S \approx 79$ K. The transition is associated with an orientational ordering of $[\text{ND}_4]^+$ tetrahedra. Two symmetry-inequivalent groups of $[\text{ND}_4]^+$ are rendered in gray and blue, respectively. Three dominant exchange interactions (J_1, J_2, J_4) are plotted as solid lines, and two sub-leading ones (J_3, J_5) are plotted as dashed lines. Antiferromagnetic J_2 and J_4 bonds form a buckled frustrated triangular-lattice planes (orange). Octahedrally coordinated local environment of Fe^{3+} atom produces a weak easy-plane magnetic anisotropy, which coincides with the ac -plane and is illustrated by orange disks on one of the four Fe^{3+} sublattices. (b) The low temperature magnetic structures of $(\text{ND}_4)_2\text{FeCl}_5 \cdot \text{D}_2\text{O}$ in zero field (cycloidal, $\mathbf{k} = (0, 0, 0.23)$) and high fields (quasi-collinear, $\mathbf{k} = (0, 0, 0)$), projected onto the ac -plane. With Transverse cycloids of spins are stabilized by competing J_2 (orange) and J_4 (green) exchanges on the buckled triangular-lattice plane. The empty and filled arrows represent spins on two parallel cycloids. Magnetic moments on sublattice 1 and 3 in the same unit cells (gray) are strictly antiparallel, so the moments on sublattice 2 and 4 across neighboring unit cells, favored by the dominant antiferromagnetic J_1 (blue) couplings. The sub-leading interaction J_5 is omitted for clarity. A spin-flop transition leads to the canted antiferromagnetic structure when an external field (≈ 5 T) is applied along \mathbf{a} at $T = 2$ K. The electric polarization switches from mostly parallel to \mathbf{a} to parallel to \mathbf{c} after the transition.

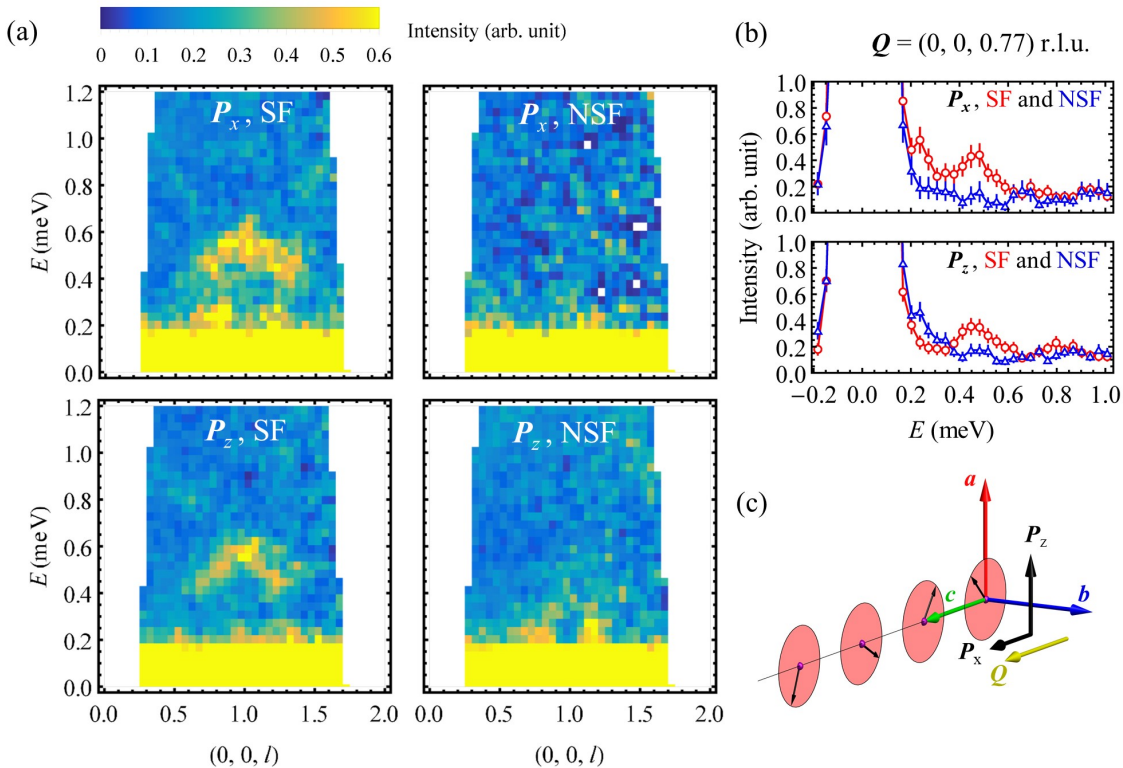


FIG. 2. Polarized neutron scattering data of $(\text{ND}_4)_2\text{FeCl}_5 \cdot \text{D}_2\text{O}$ measured at $T = 2$ K with incident neutron energy $E_i = 3.8$ meV on the HYSPEC instrument. (a) Energy-momentum slices in the spin-flip (SF) and non-spin-flip (NSF) channel with neutron polarized along the momentum transfer ($\mathbf{P}_x \parallel \mathbf{c}$) and perpendicular to the scattering plane ($\mathbf{P}_z \parallel \mathbf{a}$). (b) Constant- Q cuts at the incommensurate ordering wave-vector. (c) Schematic plot of the scattering geometry in the polarized neutron experiment, showing the cycloidal plane (pink disk), polarization of incoming neutrons (black arrows) and scattering wave-vector (yellow arrow).

active in a single material. If the multiferroic mechanism switches, does it leave a fingerprint in the microscopic magnetic interactions? In a broader context, we often think of the exchange interactions as “constants”, but in reality the lattice can distort itself in response to magnetic frustration, which in turn affects magnetic interactions through the complex interplay of various electric degrees of freedom. Different multiferroic phases of $(\text{NH}_4)_2\text{FeCl}_5 \cdot \text{H}_2\text{O}$ are readily accessible at modest fields and temperatures, providing us an excellent example to quantify such influence. Moreover, a pressure-induced multiferroic reentrant behavior was recently discovered in deuterated $(\text{ND}_4)_2\text{FeCl}_5 \cdot \text{D}_2\text{O}$ [35]. Our work on quantifying the magnetic interactions at zero pressure provides a basis for understanding such exotic behavior.

To determine the microscopic exchanges in the different multiferroic phases, we map out the entire energy and momentum dependence of excitation spectra in zero field and $B = 6$ T measuring a large deuterated single crystal sample of $(\text{ND}_4)_2\text{FeCl}_5 \cdot \text{D}_2\text{O}$ using neutrons. Deuterated sample is needed for inelastic neutron scattering measurements to reduce the incoherent scattering background from hydrogen [32]. A large single crystal of

0.6 gram was mounted on an aluminum plate and aligned in the $(0, k, l)$ scattering plane using the CG-1B alignment station at the High Flux Isotope Reactor (HFIR), Oak Ridge National Laboratory (ORNL), USA.

Two separate non-polarized experiments were performed using the same mount in zero field and applied fields on the Cold Neutron Chopper Spectrometer (CNCS) at the Spallation Neutron Source (SNS), ORNL, USA [36]. An incident energy of $E_i = 3.32$ meV in the high flux mode was used in the CNCS experiments, yielding an elastic energy resolution (FWHM) of 0.11 meV. A liquid-helium cryostat was used to cool the sample down to base temperature of $T \approx 2$ K in both the zero-field and the field experiment. An 8 T vertical cryomagnet was used in the latter experiment to supply a field up to $B = 6$ T along the a -axis of the sample. An instrumental background dataset was collected at $T = 20$ K with cryomagnet and subtracted out in data processing. No background subtraction was applied to the zero-field data. The raw event data were symmetrized according to the mmm point group of the high-temperature space group $Pnma$ and converted into a histogram format in Mantid [37]. During this process, a detector efficiency

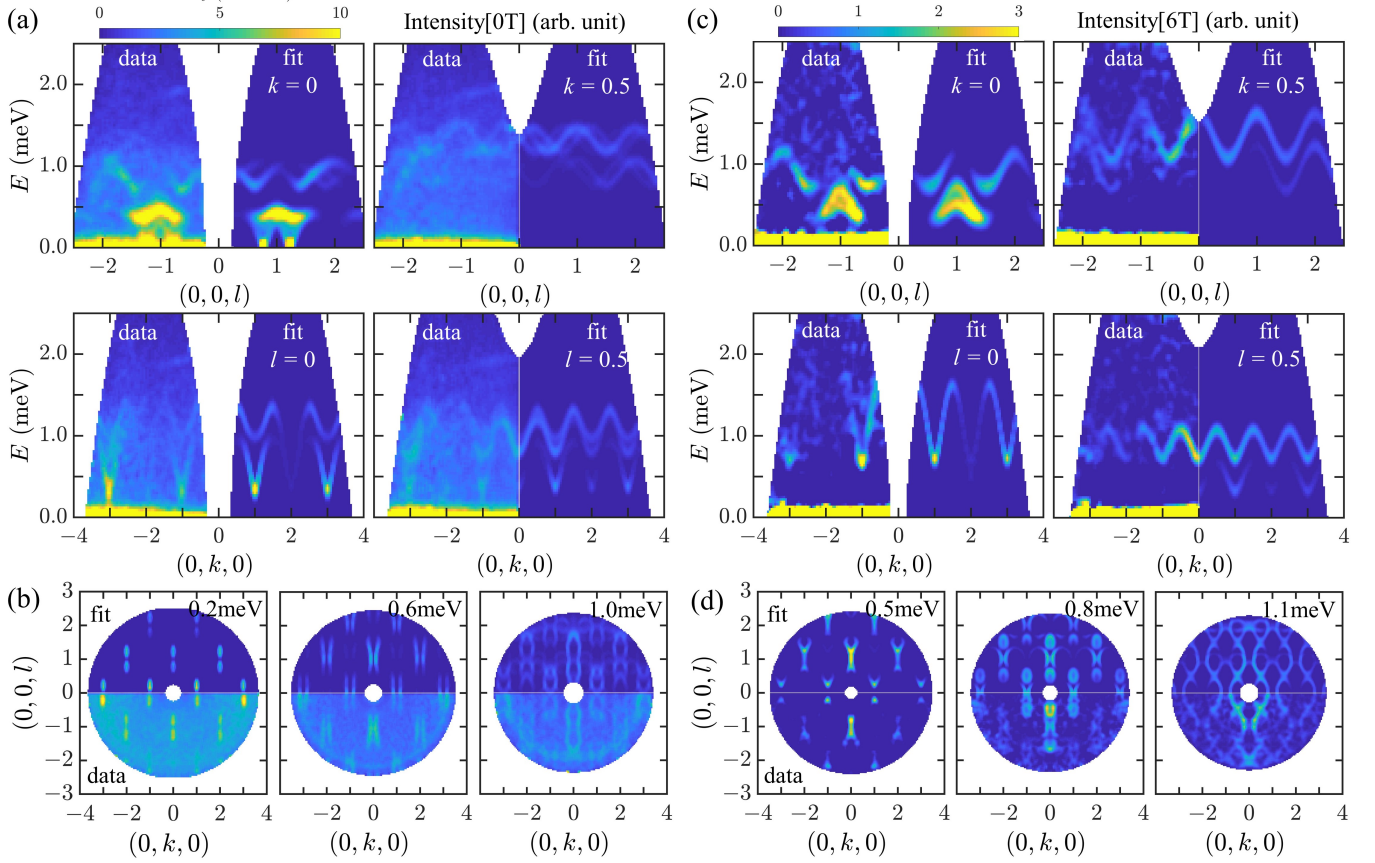


FIG. 3. Magnetic excitations of $(\text{ND}_4)_2\text{FeCl}_5 \cdot \text{D}_2\text{O}$ measured at $T = 2$ K in $B = 0$ T and 6 T applied field with incident neutron energy $E_i = 3.32$ meV on the CNCS instrument, and comparison with respective best fits using linear spin-wave theory (LSWT). (a) Representative energy-momentum slices in the $(0, k, l)$ -plane of the zero-field data and its best fitted model. An integration over $|\Delta l| \leq 0.05$ r.l.u. ($|\Delta k| \leq 0.05$ r.l.u.) is performed for constant- k ($-l$) cuts. (b) Momentum-dependence of excitation spectra of the zero-field data and the model integrated over ± 0.05 meV at selected energies. (c)(d) Similar plots for the $B = 6$ T data and its best fitted model. An integration over $|h| \leq 0.05$ r.l.u. is applied throughout all panels. The fitted background functions are not plotted for clarity.

correction using a Vanadium standard was applied. The histogram data was then imported into Horace [38] and modeled using the linear spin-wave theory (LSWT) [39] and SpinW [40].

Complementary polarized neutron scattering measurements were carried out on the Hybrid Spectrometer (HYSPEC) at SNS, ORNL, USA [41, 42]. An incident energy of $E_i = 3.8$ meV and Fermi Chopper frequency $f = 180$ Hz were used in the experiment, yielding an elastic energy resolution (FWHM) of ≈ 0.12 meV. The incident neutron beam was polarized using a vertically focusing Heusler monochromator, and the outgoing beam was analyzed using a radially collimating supermirror array. The flipping ratio was ~ 11 based on measurements of the $(0, 2, 0)$ nuclear Bragg peak. Additional neutron scattering data were collected on the Cold Neutron Triple-Axis Spectrometer (CTAX) at HFIR, ORNL, USA [Supplementary Section S1].

Before diving into the detailed modeling of the mag-

netic interactions in $(\text{ND}_4)_2\text{FeCl}_5 \cdot \text{D}_2\text{O}$, we first use the polarized neutron technique to examine the excitation spectrum in the zero-field cycloidal phase and characterize the nature of different magnetic modes. Our main observations are summarized in Fig. 2. The usual selection rule requires that only magnetic fluctuations perpendicular to the scattering wave-vector \mathbf{Q} can be detected by neutrons. In addition to this rule, the spin-flip (SF) channel in polarized neutron scattering experiments is sensitive only to magnetization components perpendicular to neutron polarization, while the non-spin-flip (NSF) scattering is sensitive only to components parallel to neutron polarization. In the \mathbf{P}_x mode where neutron is polarized along the scattering wave-vector \mathbf{Q} , scattering intensities only appear in the SF channel confirming the magnetic nature of the excitation spectra. In the \mathbf{P}_z mode where neutron polarization is perpendicular to \mathbf{Q} and the scattering plane, the scattering signals clearly split into two parts, the optical branches in the SF chan-

nel and the acoustic branches in the NSF channel. The former corresponds to fluctuations out of the cycloidal plane and along the b -axis. These modes are gapped due to additional energy cost in overcoming the easy-plane anisotropy. The latter corresponds to fluctuations along the a -axis. They are gapless modes coming from collective rotation of spins within the easy-plane, also known as phason modes.

Realistic magnetic couplings in $(\text{ND}_4)_2\text{FeCl}_5\cdot\text{D}_2\text{O}$ giving rise to the observed spectra may be quite complex. The exchange pathways up to the fifth nearest neighbors are shown in Fig. 1. At room temperature, the only symmetry of the Fe^{3+} site is a mirror plane perpendicular to the b -axis. This symmetry is broken below the structural transition at $T_S \approx 79$ K associated with $[\text{ND}_4]^+$ groups ordering in a staggered pattern along the b -axis. Consequently, all the exchange couplings, except the ones connecting the fourth neighbors, split into two symmetry-inequivalent groups, despite having almost identical bond lengths. Moreover, due to the low crystal symmetry, anisotropic exchange couplings, including symmetric interactions and antisymmetric DM interactions, are allowed on almost every bond. Only the nearest neighbor bond contains a center of inversion that prohibits DM interaction. As mentioned earlier, the spin-flop transitions take place at different critical fields when external magnetic fields are applied along \mathbf{a} and \mathbf{c} . This is presumably due to the presence of a weak anisotropy within the easy plane, which could be a subtle single-ion property created by the local environment of the Fe^{3+} site. This weak

anisotropy produces a small gap ($\sim 0.038(53)$ meV) observed in our neutron data [Supplementary Section S1]. The true value of the anisotropy gap can not be obtained reliably from our data due to the strong temperature damping effect.

Nevertheless, to make progress in quantifying magnetic interactions of $(\text{ND}_4)_2\text{FeCl}_5\cdot\text{D}_2\text{O}$, we keep complexity of the model at minimum and introduce a Heisenberg Hamiltonian in a magnetic field with an easy-plane anisotropy,

$$\mathcal{H} = \sum_{i,j} J_{ij} \mathbf{S}_i \cdot \mathbf{S}_j + D \sum_i (S_i^y)^2 + gB \sum_i S_i^x, \quad (1)$$

where \mathbf{S}_i is the spin operator of Fe^{3+} ion on site i with length $S = 5/2$, D is the single-ion anisotropy and $g = 2$ is the electron g-factor. Here we neglect the lattice distortion and assume that the ac -plane is a mirror plane and the magnetic easy-plane. The weak anisotropy within the easy-plane is neglected as well. We perform two independent pixel-to-pixel fitting to the entire volume of 4-dimensional (h, k, l, E) data collected in the zero-field cycloidal phase, and a volume of 3-dimensional (k, l, E) data collected in the canted antiferromagnetic phase of $B = 6$ T. Due to the narrow opening of the vertical magnet, the momentum transfer along h is limited and integrated over $|h| < 0.05$ r.l.u. in analysis of the field data. A linear background as a function of energy is included in fitting each dataset. The calculated spectra are convoluted with instrumental resolution (FWHM ≈ 0.11 meV).

$$J_4 = \frac{1}{2 \sin(2\pi k_c)} (2J_2 \sin(2\pi k_c/2) + J_1 \sin(2\pi k_c/2 - \phi) + J_3 \sin(2\pi k_c/2 + \phi)) \quad (2)$$

$$J_5 = -(J_1 - J_3) \sin(2\pi k_c/2) / \tan(\phi) + (J_1 + J_3) \cos(2\pi k_c/2) \quad (3)$$

In zero field, we obtain two analytic constraints of exchange parameters, Eq.(2) and (3), for stabilizing the cycloid spin structure in $(\text{ND}_4)_2\text{FeCl}_5\cdot\text{D}_2\text{O}$. The exchange parameters J_4 and J_5 are solved on-the-fly in the fitting, using the observed incommensurate wave vector k_c and phase difference ϕ between sublattice 1 and 4. The source of frustration comes from antiferromagnetic J_2 and J_4 on the buckled triangular-lattice plane. Setting all the other exchanges to zero, we recover the well-known result for stabilizing a spiral structure with $2\pi k_c = 2 \arccos(J_2/(2J_4))$ in the Heisenberg model on an anisotropic triangular lattice. The relative phase difference ϕ of cycloids on different sublattices in $(\text{ND}_4)_2\text{FeCl}_5\cdot\text{D}_2\text{O}$ is tuned by the exchange parameters J_1, J_3 and J_5 . Additional fittings are performed for ϕ in the range of 30° to 48° , Fig. S8. The fitting quality shows strong dependence on the phase difference. The optimal

value of ϕ is around 39° , reasonably close to the experimental value of 41.5° . To avoid any bias in determining the model parameters in high-field phase, no constraints are applied in fitting the $B = 6$ T data. The comparison between experimental data and corresponding fits is presented in Fig. 3 for selected cuts. See Supplementary Section S2 for more details. The agreement is fairly good for both phases across all reciprocal space detected in the experiments. The best fitting parameters are summarized in Tab. I.

Several important conclusions can be drawn from our detailed LSWT modelling. First, we find notable differences beyond estimated errors between the best model parameters for the zero-field and the high-field data, roughly on the level of 10% for exchange interactions. The single-ion anisotropy, as the weakest term among all, shows a significant $\sim 50\%$ increase compared to the

B (T)	J_1 (meV)	J_2	J_3	J_4	J_5	D	χ_{0T}^2	χ_{6T}^2	k_c	ϕ ($^\circ$)	θ ($^\circ$)
0.0	0.1710(1)	0.05871(6)	0.02985(4)	0.0535 [‡]	0.0461 [‡]	0.01043(3)	29.20	1.84*	0.23 [†]	41.50 [†]	12.60*
6.0	0.1801(2)	0.05313(14)	0.03198(15)	0.05535(11)	0.04001(8)	0.01543(6)	30.00*	1.15	0.24*	42.44*	12.61
diff.	0.0091	-0.00558	0.00213	0.00185	-0.00609	0.005	0.8	-0.69	0.01	0.94	0.01

TABLE I. Values of the best fitting parameters for $(\text{ND}_4)_2\text{FeCl}_5\cdot\text{D}_2\text{O}$ in two different multiferroic phases. [†] parameters, the incommensurate ordering wave-vector k_c and the phase difference ϕ between spin on sublattice 1 and 4, are fixed in fitting of the zero-field data. [‡] parameters, J_4 and J_5 , are calculated on-the-fly using Eq. (2) and (3). * values are computed using respectively optimal fitting parameters. The large χ^2 for the zero-field data is due to incoherent backgrounds that can not be fully accounted for. The parameter θ is the canting angle of spin on sublattice 2 from the crystallographic c -axis. The single-ion anisotropy in the 6 T model increases by $\sim 50\%$ compared to that of the zero-field model, while the differences of individual exchange constants are around 10% between two models.

value in zero field. We compute the reduced χ^2 for the 0 T (6 T) data using the 6 T (0 T) model parameters, keeping the optimal background parameters. The result shows that deviation from the optimal model parameters does produce a meaningful difference in the quality of the fit. One caveat though is that some of the exchange parameters show significant correlations and corresponding errors might be underestimated, Fig. S9. The single-ion anisotropy in comparison has very little correlation with the other parameters.

Second, despite the observed differences in the best fitted parameter values, these two models have very similar ground state properties. We cross-check the incommensurate ordering wave-vector k_c and the phase difference ϕ of the 0 T cycloidal phase using the 6 T model parameters and do not find significant difference from the experimental values (fixed in fitting the zero-field data). Vice versa, we compute the canting angle θ at 6 T using the 0 T model and obtain almost identical result as the 6 T model. Moreover, we find the saturation magnetic field to be ~ 27.5 T from both models, reasonably close to the experimental value of $B_{\text{sat}} \approx 30$ T [29]. Third, the fitted values of J_2 and J_4 are very close, indeed giving rise to expected magnetic frustration. This is in sharp contrast with models of $\text{K}_2\text{FeCl}_5\cdot\text{H}_2\text{O}$ extracted from inelastic neutron data [43], where J_4 is significantly smaller than J_2 . Therefore, a collinear structure instead of cycloid is stabilized at zero field in this compound [44]. The presence of ammonium groups is closely related to the enhancement of J_4 and the magnetic frustration in the system. A recent neutron diffraction study under pressure suggests that a moderate external pressure may alter the conformation of ammonium groups and produce novel multiferroic reentrant phenomenon in $(\text{ND}_4)_2\text{FeCl}_5\cdot\text{D}_2\text{O}$ [35].

In this work, we conduct a systematic inelastic neutron scattering study of molecule-based multiferroic compound $(\text{ND}_4)_2\text{FeCl}_5\cdot\text{D}_2\text{O}$ in the zero-field cycloidal phase and the high-field canted antiferromagnetic phase. The best model parameters show notable differences in exchange “constants” between these models, however no qualitative change is observed in the ground state prop-

erties of the system. The electric polarization measurements of $(\text{ND}_4)_2\text{FeCl}_5\cdot\text{D}_2\text{O}$ suggests a switch of multiferroic mechanism from the inverse DM model to the p - d hybridization model between the zero-field phase and the high-field phase, therefore one might expect more drastic changes in the underlying magnetic couplings. Yet, our result suggests that magnetic exchange interactions in $(\text{ND}_4)_2\text{FeCl}_5\cdot\text{D}_2\text{O}$ are much more robust than electric polarization in response to delicate reorganizations of electronic degrees of freedom under an external magnetic field. Alternatively, it is worth noting that the field-induced magnetostriction effect could also alter exchange interactions [45], and it has been shown to take place in the transition to the high-field phase in this compound [28], hence remains as a strong contender in providing an unified picture of multiferroic behavior of $(\text{ND}_4)_2\text{FeCl}_5\cdot\text{D}_2\text{O}$ in future studies.

We thank Feng Ye and Clarina dela Cruz for valuable discussion, and Andrei Savici for the help in data reduction. X.B. and H.B.C acknowledges the support of US DOE BES Early Career Award KC0402010 under Contract DE-AC05-00OR22725. R.S.F. is supported by the U.S. Department of Energy, Office of Basic Energy Sciences, Materials Sciences and Engineering Division. This research used resources at the High Flux Isotope Reactor and Spallation Neutron Source, a DOE Office of Science User Facility operated by the Oak Ridge National Laboratory.

* baix@ornl.gov

† wt6@ornl.gov

- [1] M. Fiebig, Journal of physics D: applied physics **38**, R123 (2005).
- [2] H. Schmid, Ferroelectrics **162**, 317 (1994).
- [3] F. Kubel and H. Schmid, Acta Crystallographica Section B: Structural Science **46**, 698 (1990).
- [4] I. Sosnowska, T. P. Neumaier, and E. Steichele, Journal of Physics C: Solid State Physics **15**, 4835 (1982).
- [5] S.-W. Cheong and M. Mostovoy, Nature materials **6**, 13 (2007).

- [6] D. Khomskii, “Classifying multiferroics: mechanisms and effects. physics (college park md),” (2009).
- [7] H. Walker, F. Fabrizi, L. Paolasini, F. de Bergevin, J. Herrero-Martin, A. Boothroyd, D. Prabhakaran, and D. McMorrow, *Science* **333**, 1273 (2011).
- [8] I. A. Sergienko and E. Dagotto, *Phys. Rev. B* **73**, 094434 (2006).
- [9] T. Kimura, T. Goto, H. Shintani, K. Ishizaka, T.-h. Arima, and Y. Tokura, *nature* **426**, 55 (2003).
- [10] Y. Yamasaki, H. Sagayama, T. Goto, M. Matsuura, K. Hirota, T. Arima, and Y. Tokura, *Physical review letters* **98**, 147204 (2007).
- [11] A. Narayan, A. Cano, A. V. Balatsky, and N. A. Spaldin, *Nature materials* **18**, 223 (2019).
- [12] H. Xiang, S.-H. Wei, M.-H. Whangbo, and J. L. Da Silva, *Phys. Rev. Lett.* **101**, 037209 (2008).
- [13] A. Malashevich and D. Vanderbilt, *Phys. Rev. Lett.* **101**, 037210 (2008).
- [14] M. Kenzelmann, A. B. Harris, S. Jonas, C. Broholm, J. Schefer, S. Kim, C. Zhang, S.-W. Cheong, O. P. Vajk, and J. W. Lynn, *Phys. Rev. Lett.* **95**, 087206 (2005).
- [15] S. Lovesey, V. Scagnoli, M. Garganourakis, S. Koohpayeh, C. Dettlefs, and U. Staub, *Journal of Physics: Condensed Matter* **25**, 362202 (2013).
- [16] I. Solovyev, *Phys. Rev. B* **83**, 054404 (2011).
- [17] K. Taniguchi, N. Abe, T. Takenobu, Y. Iwasa, and T. Arima, *Phys. Rev. Lett.* **97**, 097203 (2006).
- [18] G. Lawes, A. B. Harris, T. Kimura, N. Rogado, R. J. Cava, A. Aharony, O. Entin-Wohlman, T. Yildirim, M. Kenzelmann, C. Broholm, *et al.*, *Phys. Rev. Lett.* **95**, 087205 (2005).
- [19] R. Villarreal, G. Quirion, M. Plumer, M. Poirier, T. Usui, and T. Kimura, *Phys. Rev. Lett.* **109**, 167206 (2012).
- [20] H. Xiang and M.-H. Whangbo, *Phys. Rev. Lett.* **99**, 257203 (2007).
- [21] K. Wang, J.-M. Liu, and Z. Ren, *Advances in Physics* **58**, 321 (2009).
- [22] O. M. Yaghi, M. O’Keeffe, N. W. Ockwig, H. K. Chae, M. Eddaoudi, and J. Kim, *Nature* **423**, 705 (2003).
- [23] R. Samantaray, R. J. Clark, E. S. Choi, and N. S. Dalal, *Journal of the American Chemical Society* **134**, 15953 (2012).
- [24] G.-C. Xu, W. Zhang, X.-M. Ma, Y.-H. Chen, L. Zhang, H.-L. Cai, Z.-M. Wang, R.-G. Xiong, and S. Gao, *Journal of the American Chemical Society* **133**, 14948 (2011).
- [25] R. Samantaray, R. J. Clark, E. S. Choi, H. Zhou, and N. S. Dalal, *Journal of the American Chemical Society* **133**, 3792 (2011).
- [26] M. Ackermann, T. Lorenz, P. Becker, and L. Bohatý, *Journal of Physics: Condensed Matter* **26**, 506002 (2014).
- [27] R. Carlin, S. Bhatia, and C. O’Connor, *Journal of the American Chemical Society* **99**, 7728 (1977).
- [28] M. Ackermann, D. Brünig, T. Lorenz, P. Becker, and L. Bohatý, *New Journal of Physics* **15**, 123001 (2013).
- [29] A. J. Clune, J. Nam, M. Lee, K. D. Hughey, W. Tian, J. A. Fernandez-Baca, R. S. Fishman, J. Singleton, J. H. Lee, and J. L. Musfeldt, *npj Quantum Materials* **4**, 1 (2019).
- [30] J. A. Rodríguez-Velamazán, Ó. Fabelo, Á. Millán, J. Campo, R. D. Johnson, and L. Chapon, *Scientific reports* **5**, 14475 (2015).
- [31] J. A. Rodríguez-Velamazán, Ó. Fabelo, J. Campo, Á. Millán, J. Rodríguez-Carvajal, and L. C. Chapon, *Phys. Rev. B* **95**, 174439 (2017).
- [32] W. Tian, H. Cao, J. Wang, F. Ye, M. Matsuda, J.-Q. Yan, Y. Liu, V. O. Garlea, H. K. Agrawal, B. C. Chakoumakos, *et al.*, *Phys. Rev. B* **94**, 214405 (2016).
- [33] D. Brünig, T. Fröhlich, M. Langenbach, T. Leich, M. Meven, P. Becker, L. Bohatý, M. Grüninger, M. Braden, and T. Lorenz, *arXiv preprint arXiv:2001.11780* (2020).
- [34] J. A. Rodríguez-Velamazán, Ó. Fabelo, J. Campo, J. Rodríguez-Carvajal, N. Qureshi, and L. C. Chapon, *Scientific reports* **8**, 1 (2018).
- [35] Y. Wu, D. Lei, Y. Cheng, N. Su, N. Ma, K. Zhai, B. C. Chakoumakos, Y. Sun, J. Cheng, W. Tian, and H. Cao, *In preparation*.
- [36] G. Ehlers, A. A. Podlesnyak, J. L. Niedziela, E. B. Iverson, and P. E. Sokol, *Review of Scientific Instruments* **82**, 085108 (2011).
- [37] O. Arnold, J.-C. Bilheux, J. Borreguero, A. Buts, S. I. Campbell, L. Chapon, M. Doucet, N. Draper, R. F. Leal, M. Gigg, *et al.*, *Nuclear Instruments and Methods in Physics Research Section A: Accelerators, Spectrometers, Detectors and Associated Equipment* **764**, 156 (2014).
- [38] R. Ewings, A. Buts, M. Le, J. van Duijn, I. Bustinduy, and T. Perring, *Nuclear Instruments and Methods in Physics Research Section A: Accelerators, Spectrometers, Detectors and Associated Equipment* **834**, 132 (2016).
- [39] R. S. Fishman, J. A. Fernandez-Baca, and T. Rõm, *Spin-Wave Theory and its Applications to Neutron Scattering and THz Spectroscopy* (Morgan & Claypool Publishers, 2018).
- [40] S. Toth and B. Lake, *Journal of Physics: Condensed Matter* **27**, 166002 (2015).
- [41] M. B. Stone, J. L. Niedziela, D. L. Abernathy, L. DeBeer-Schmitt, G. Ehlers, O. Garlea, G. Granroth, M. Graves-Brook, A. I. Kolesnikov, A. Podlesnyak, *et al.*, *Review of Scientific Instruments* **85**, 045113 (2014).
- [42] B. Winn, U. Filges, V. O. Garlea, M. Graves-Brook, M. Hagen, C. Jiang, M. Kenzelmann, L. Passell, S. M. Shapiro, X. Tong, *et al.*, in *EPJ Web of Conferences*, Vol. 83 (EDP Sciences, 2015) p. 03017.
- [43] J. Campo, J. Luzon, F. Palacio, G. J. McIntyre, A. Millan, and A. R. Wildes, *Phys. Rev. B* **78**, 054415 (2008).
- [44] M. Gabás, F. Palacio, J. Rodríguez-Carvajal, and D. Visser, *Journal of Physics: Condensed Matter* **7**, 4725 (1995).
- [45] Y. Shapira and N. Oliveira Jr, *Physical Review B* **18**, 1425 (1978).

Supplementary Information

S1. COMPLIMENTARY TRIPLE-AXIS NEUTRON SCATTERING DATA

The CTAX experiment was performed with a fixed final neutron energy of $E_f = 3.5$ meV, yielding an elastic energy resolution (HWHM) of ≈ 0.1 meV. The higher harmonic neutrons were removed by the cooled Be filter placed between the sample and the analyzer. The collimation of guide-open-sample-80'-open was used throughout the experiment.

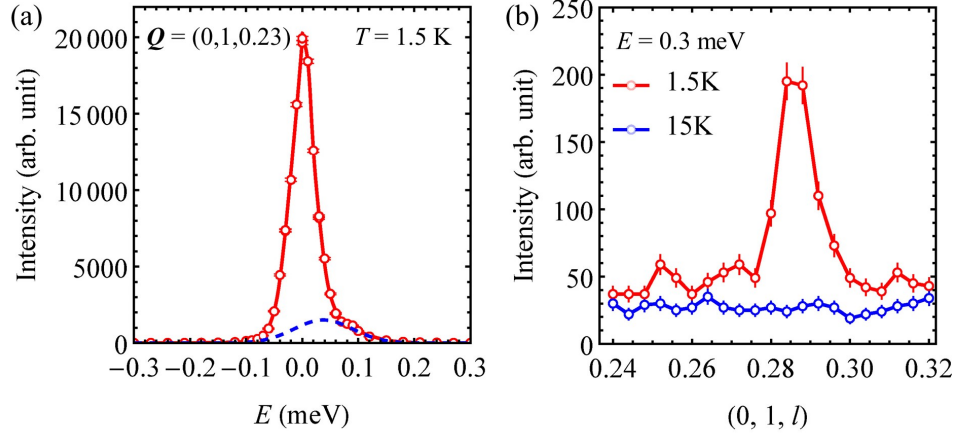


FIG. S1. (a) Constant- \mathbf{Q} scan at the magnetic Bragg peak $(0, 1, 0.23)$. A broad shoulder indicates possible existence of a gap due to anisotropy within the ac -plane. The fitted peak (blue dashed curve) is centered around 0.0376 meV with a FWHM of 0.1237 meV, much larger than the FWHM (0.0563 meV) of the elastic peak (red curve). The true value of the anisotropy gap is difficult to estimate due to the strong temperature damping effect. (b) Temperature dependence of constant-energy scans at $E = 0.3$ meV measured along $(0, 1, l)$ at $T = 1.5$ and 15 K. The lines are guide for the eye.

S2. COMPARISON BETWEEN DATA AND LINEAR SPIN WAVE THEORY MODELING

To elucidate the overall quality of the modeling, we show detailed cuts across reciprocal space comparing the zero-field data (Fig. S2-S4) and $B = 6$ T data (Fig. S5-S7) with respective best LSWT fits. See main text for details of instrumental setup. The fitted background functions are not plotted for clarity.

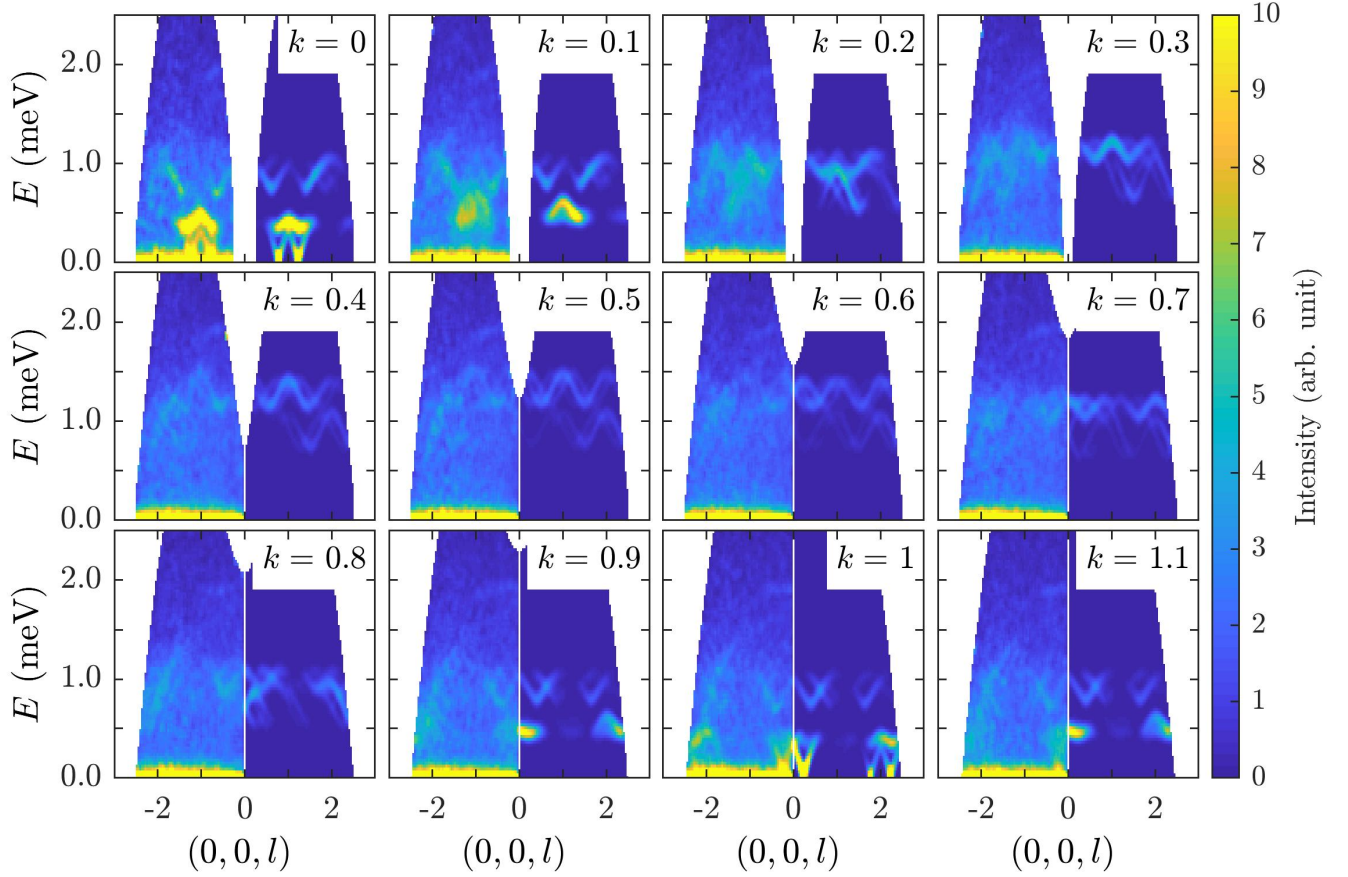


FIG. S2. Comparison between the zero-field data in the $(0, k, l)$ -plane and its best fitted model. In each panel, the data is shown on the left and the fit on the right, integrated over $|\Delta k| \leq 0.05$ r.l.u. and $|h| \leq 0.05$ r.l.u..

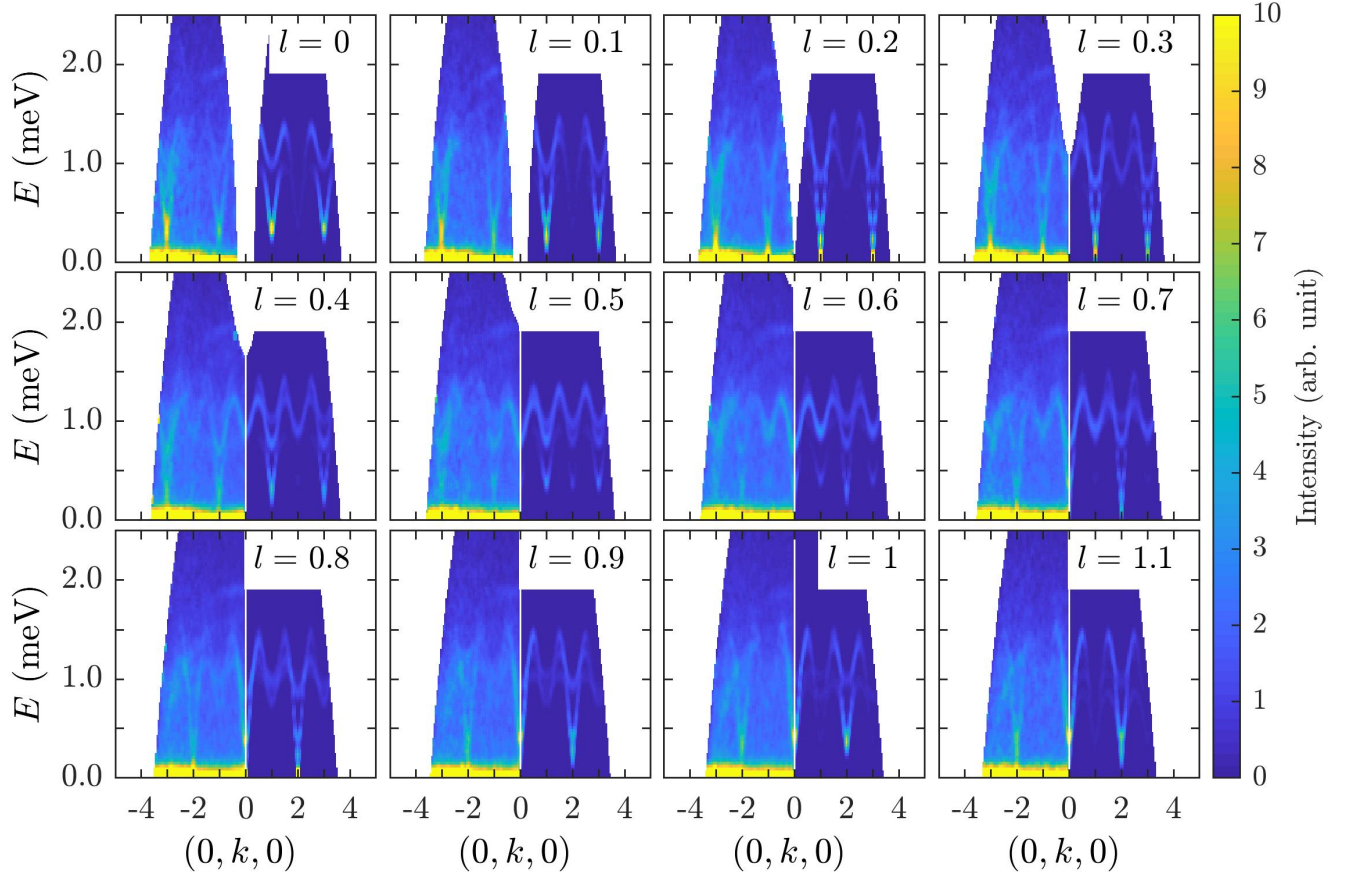


FIG. S3. Comparison between the zero-field data in the $(0, k, l)$ -plane and its best fitted model. In each panel, the data is shown on the left and the fit on the right, integrated over $|\Delta l| \leq 0.05$ r.l.u. and $|h| \leq 0.05$ r.l.u..

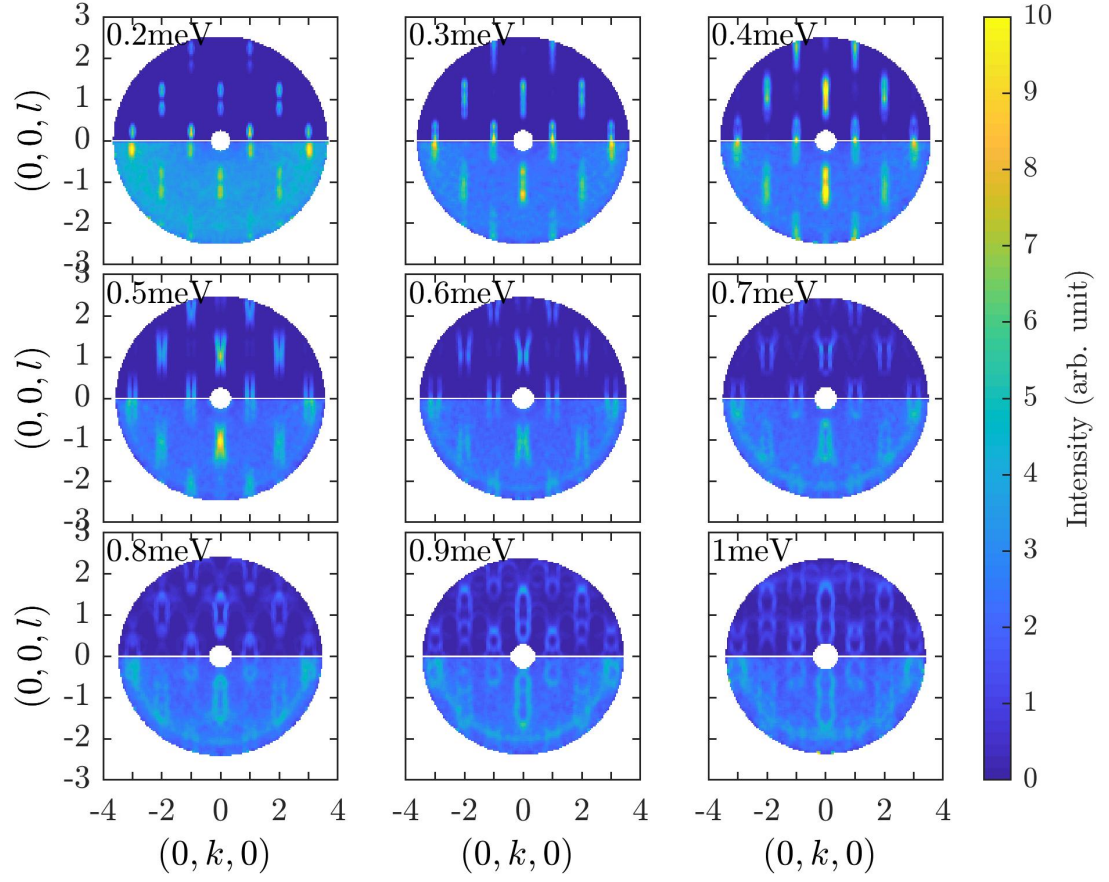


FIG. S4. Momentum-dependence of excitation spectra of the zero-field data and the model integrated over $|\Delta E| \leq 0.05$ meV at selected energies indicated at the top-left corner of each panel. The data is shown on the bottom half of each panel and the fit on the top half.

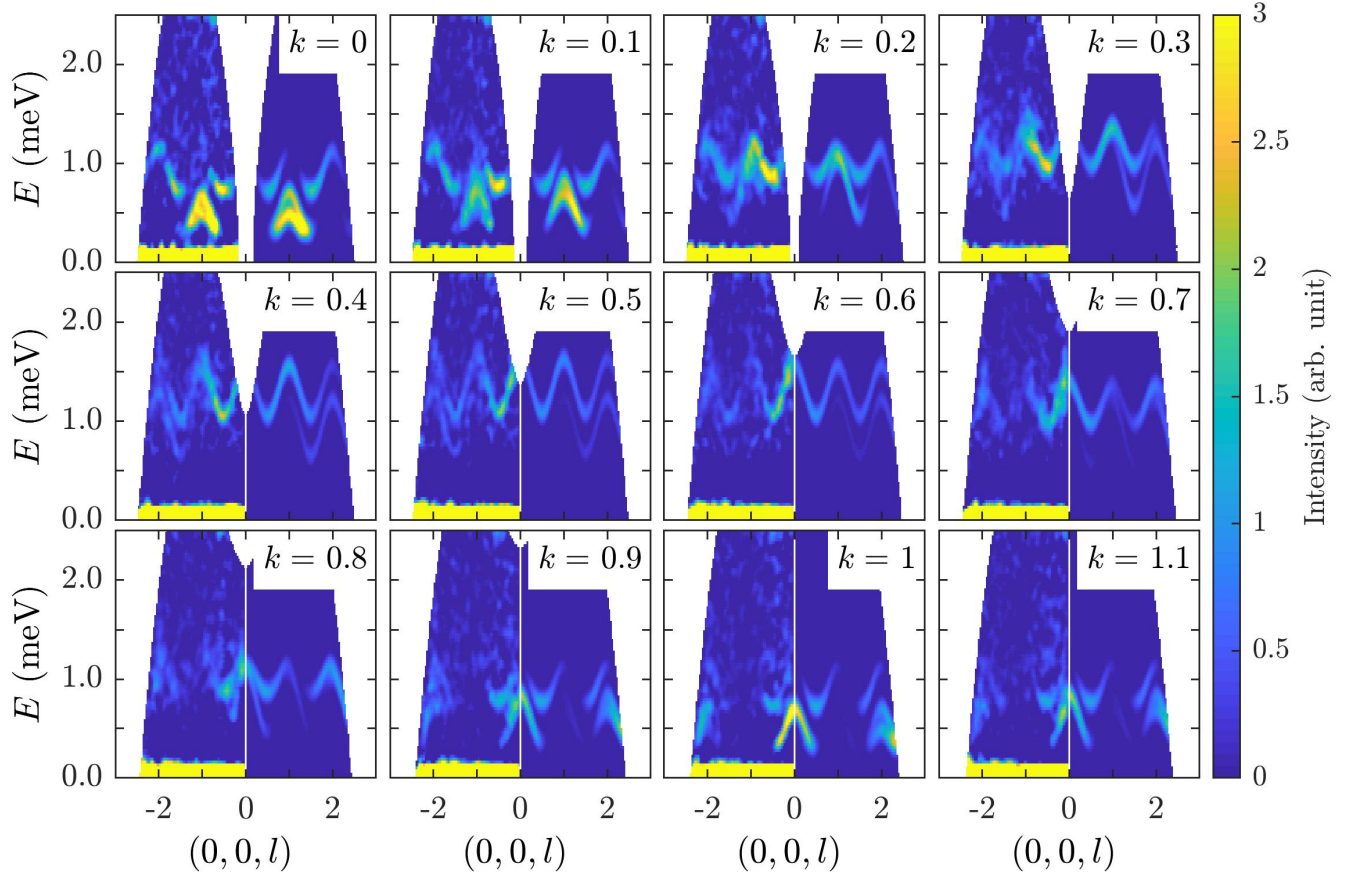


FIG. S5. Comparison between the $B = 6$ T data in the $(0, k, l)$ -plane and its best fitted model. In each panel, the data is shown on the left and the fit on the right, integrated over $|\Delta k| \leq 0.05$ r.l.u. and $|h| \leq 0.05$ r.l.u..

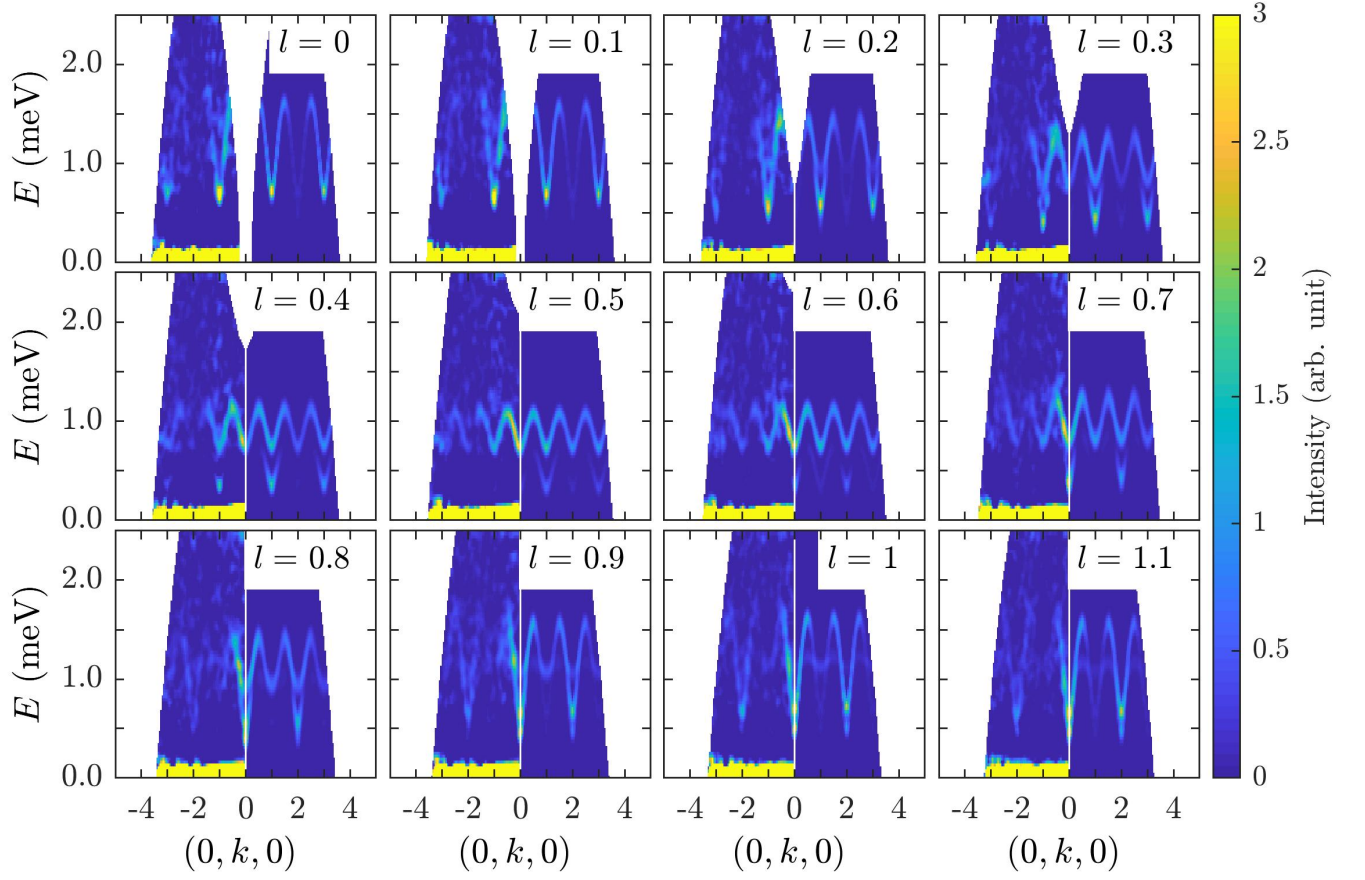


FIG. S6. Comparison between the $B = 6$ T data in the $(0, k, l)$ -plane and its best fitted model. In each panel, the data is shown on the left and the fit on the right, integrated over $|\Delta l| \leq 0.05$ r.l.u. and $|h| \leq 0.05$ r.l.u..

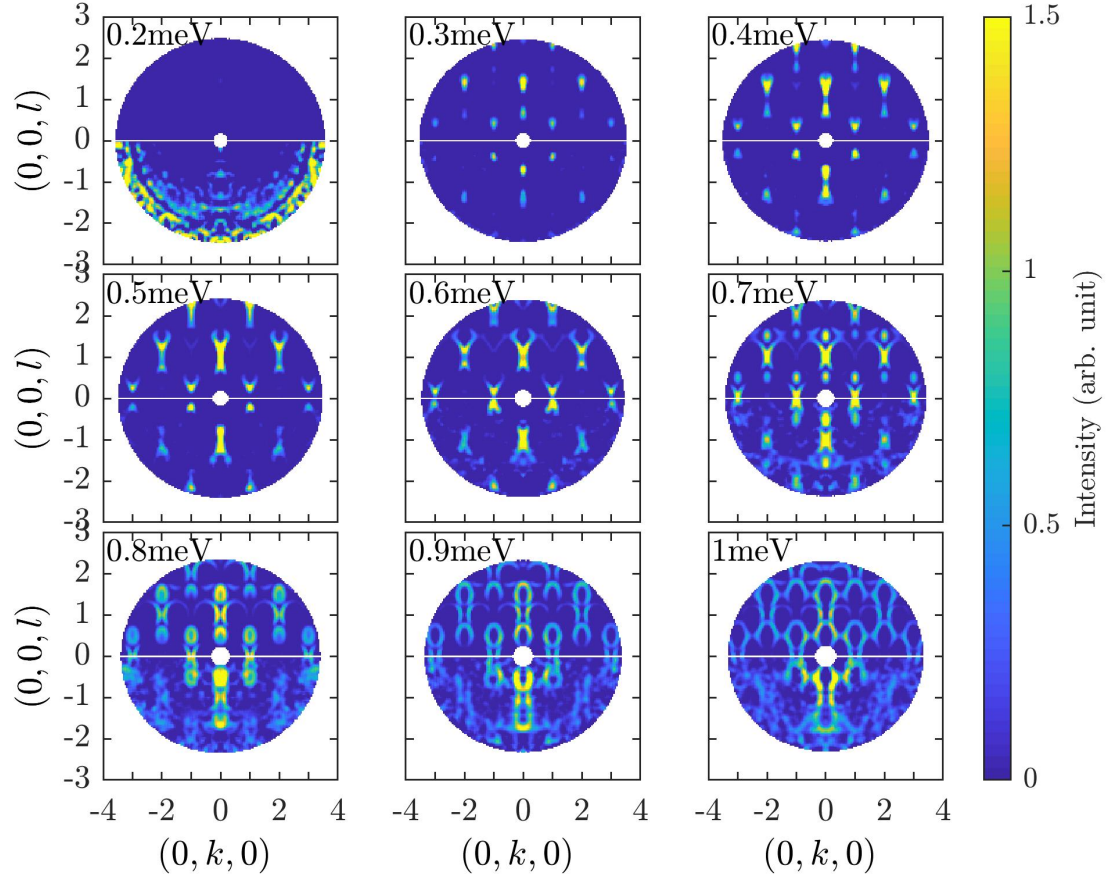


FIG. S7. Momentum-dependence of excitation spectra of the $B = 6$ T data and the model integrated over $|\Delta E| \pm 0.05$ meV at selected energies indicated at the top-left corner of each panel. The data is shown on the bottom half of each panel and the fit on the top half.

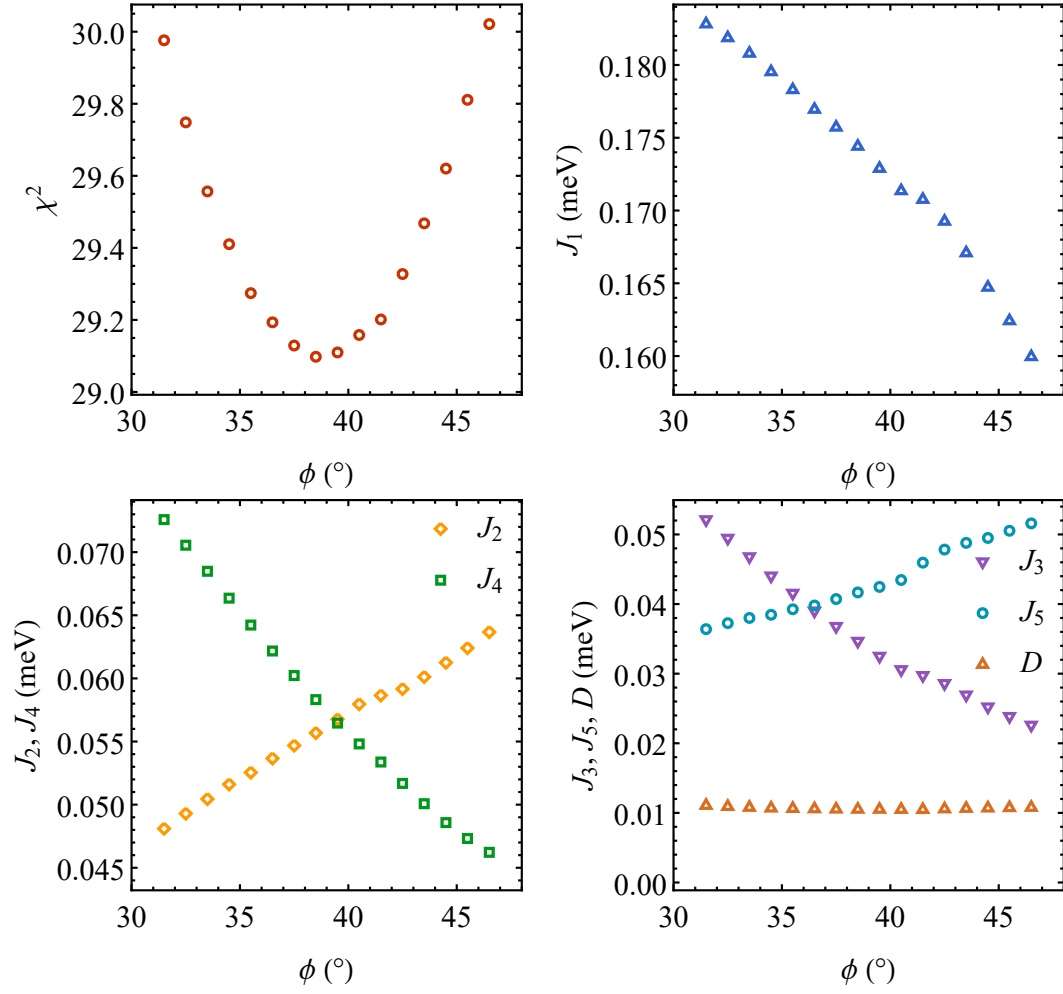


FIG. S8. The reduced χ^2 and the optimal model parameters as a function of the phase difference ϕ , obtained from fitting the zero-field data. The minimal χ^2 corresponds to a phase difference $\phi \approx 39^\circ$, reasonably close to the value reported in neutron diffraction studies, 41.5° .

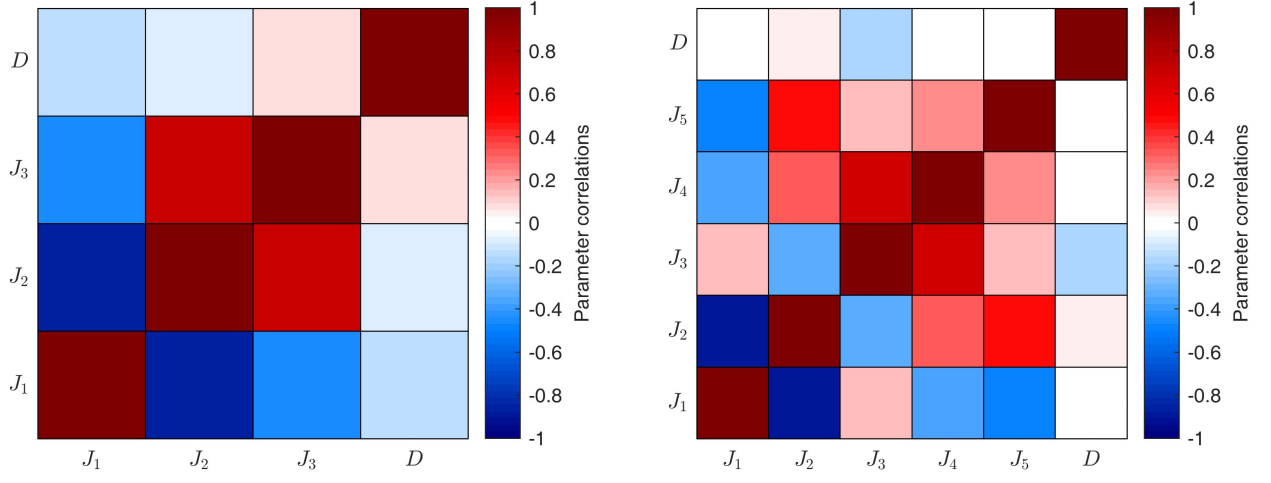


FIG. S9. Parameter correlations for the zero-field model (Left) and the high-field model (Right).